ADVANCED FUNCTIONAL MATERIALS
www.afm-journal.de

Fluoride-Free Molten Salt Hydrate-Assisted Synthesis of MXene in Air Down to 150 °C

*Sin-Yi Pang, Weng Fu Io, Lok-Wing Wong, Xinyue Lao, Qianqian Bai, Kam Lin Chan, Jiong Zhao, and Jianhua Hao**

The conventional Lewis acid molten salt etching approach for synthesizing MXenes typically necessitates elevated temperatures exceeding 550 °C, in addition to the use of inert gas protection to prevent oxidation. Additionally, delamination of molten salt-etched MXenes typically requires hazardous intercalating agents. Herein, a scalable and non-toxic low-temperature shielded salt (LSS) approach for synthesizing MXene in air is reported, with the use of only a small portion of salts and a low reaction temperature down to 150 °C. Especially, the synergistic effect of the increased diffusion rate by Li^+ ions and the phase change of magnesium chloride hexahydrate ($MgCl_2 \cdot 6H_2O$) enables a redox-controlled A-site etching of the parent MAX phase, which even facilitates the synthesis of hard-to-etch MXenes. As a proof-of-concept demonstration, several theoretically hard-to-synthesize MXenes including Cr_2CT_x and Nb_2CT_x are successfully prepared through the LSS technique, where Cr_2CT_x is not achieved by Lewis acidic molten salt yet. Compared to conventional techniques, this low-temperature shielded salt etching method exhibits unconventional molten behavior while offering several advantages, including a non-oxidizing environment, shorter processing time, and elimination of highly corrosive washing agents and organic intercalants. These advances render the LSS approach a promising route for synthesizing MXenes with applications toward diverse practical applications.

1. Introduction

Emerging two-dimensional (2D) transition metal carbides, nitrides, and carbonitrides, known as MXene, exhibit a wide range of applications including battery, electrochemical energy storage, and biosensor, owing to their layered structure, metallic conductivity, and low cytotoxicity.[1–5] MXene is commonly fabricated through the selective etching of the "A" layer components from the parent MAX phase using a solution containing fluoride or through the assistance of molten salt or alkali under high temperature and pressure.[6–8] In MAX phase material, the "M" represents an early transition metal element (such as Ti, V, Cr, etc.), "A" represents an element from groups 13–16 (such as Al, Si, etc.) and X is C and/or N. The chemical component of MXene is $M_{n+1}X_nT_x$ (n = 1,2,3), where T_x denotes the surface termination, such as oxygen, hydroxyl, and halogen groups.[9–11]

Lewis acidic molten salt (LAMS) etching route is a developing method to prepare HF-free MXene by utilizing various metal salts.[7] LAMS-etched HF-free MXenes have attracted attention due to their controllable surface chemistry with unique features such as outstanding capacitance[6] and superconductivity.[12] The utilization of a hydrofluoric acid-free synthesis protocol can eliminate the hazard associated with the use of toxic hydrofluoric acid, a highly corrosive and hazardous agent, thereby minimizing the safety concerns linked to the etching process.[13–15] However, achieving successful exfoliation of MXene in the molten salt requires critical conditions such as high temperature (>550 °C) and an argon atmosphere to protect the material from oxidation.[16] The elevated temperatures required during the conventional synthesis process can lead to oxidation of the material and additional processing time is needed to reach the target high-temperature regime.[17–18] Recent progress has been made in the delamination of LAMS-MXenes using LiCl in anhydrous polar organic solvents,[19–21] which resolves issues related to previously used hazardous chemicals such as n-butyllithium. Despite these advances, the high-temperature synthesis conditions remain, and the current molten salt synthesis approach has only been applied to a few MXene members. The feasibility of synthesizing certain MXenes, such as Cr_2C, which are theoretically predicted to be difficult to exfoliate, has not been explored using the LAMS etching method.[22] On the other hand, the Molten Salt Shielded Synthesis/Sintering (MS^3) approach leverages molten salts as both a reaction medium and a protective agent for MXene, shielding it

S.-Y. Pang, W. F. Io, L.-W. Wong, X. Lao, Q. Bai, K. L. Chan, J. Zhao, J. Hao
Department of Applied Physics
The Hong Kong Polytechnic University
Hong Kong 999077, China
E-mail: jh.hao@polyu.edu.hk

J. Hao
Research Centre for Nanoscience and Nanotechnology
The Hong Kong Polytechnic University
Hong Kong 999077, China

The ORCID identification number(s) for the author(s) of this article can be found under https://doi.org/10.1002/adfm.202504864

DOI: 10.1002/adfm.202504864

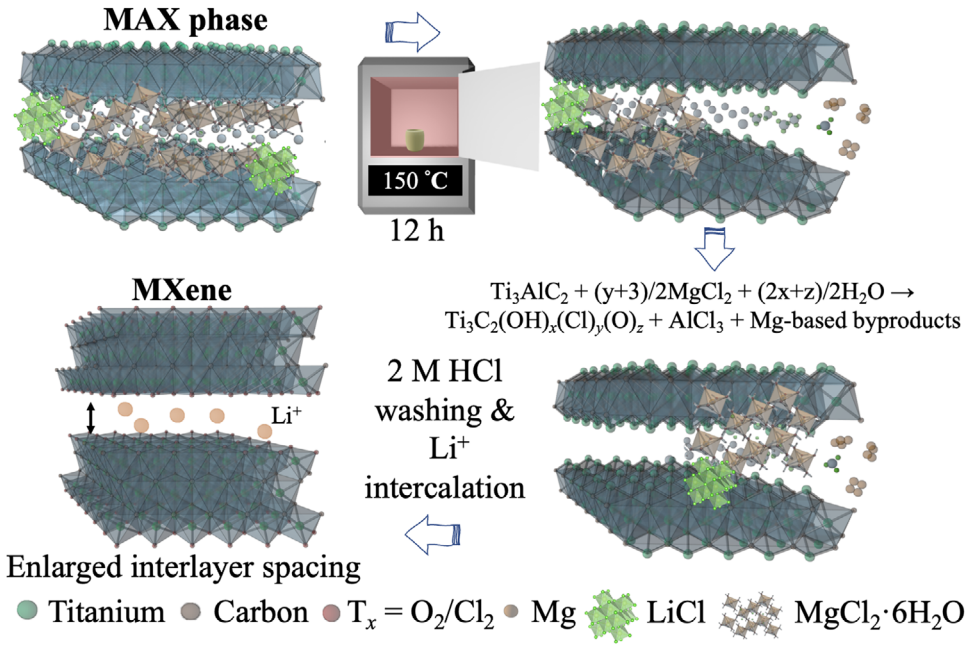

Figure 1. The schematic diagram depicts the LSS process. This synthesis involves a redox reaction on the A-site of the MAX phase material, resulting in the termination of functionalized groups on the resulting MXene.

from oxidation during high-temperature processing in ambient air conditions.[21,23–25] This approach enables a reduced etching duration at a high reaction temperature of 700 °C and helps to prevent direct exposure of the oxidation-prone materials to ambient air.[24,26] Despite the potential of using salt to lower the reaction temperature through the dissolution-precipitation route, research on utilizing lower temperatures for etching is very limited, and fluoride-containing molten salt is needed.[23,27]

In this study, we present a facile and fluoride-free approach for etching MXene materials through a low-temperature shielded salt (LSS) method operating below 150 °C in air, in which the fabricated MXene is terminated with —Cl, =O, and —OH functional groups and holds an obvious delamination without using extra intercalator. Without using an oxidizing washing agent and a low-temperature environment, the oxidization of the surface of MXene to TiO_2 can be avoided. The decreased temperature and the used amount of salt for the LSS reaction, as well as the incorporation of the shielding effect, also yield cost-saving benefits through reduced processing time and the employment of a more economical etchant. As a proof-of-concept experiment, multiple hard-to-synthesize MXenes including Cr_2CT_x were successfully etched through our LSS approach and demonstrated as catalysts for hydrogen evolution reaction (HER). Impressively, the pristine Cr_2CT_x exhibits a low overpotential of 186 mV at a specific current density of 10 mA^{-2}. Our LSS method not only provides a simple and non-toxic means of delaminating MXene nanoflakes at a much lower temperature of 150 °C in air but also enables the synthesis of MXene materials that are theoretically difficult to prepare using conventional approaches. This advancement will foster further research into the synthesis of MXenes and the investigation of their material properties, promising expanded applications, especially in environments sensitive to fluoride or toxins.

2. Result and Discussion

2.1. Synthesis and Characterization of Titanium Carbide by LSS Method

$Ti_3C_2T_x$ was selected as the prototype for synthesizing fluorine-free MXene due to the extensive research conducted on Ti_3C_2 across diverse applications and analyses, including electrocatalytic applications and Raman spectroscopic studies.[28–29] First, Ti_3AlC_2 is immersed in $MgCl_2{\cdot}6H_2O$/LiCl mixed salt and heated at 150 °C, as illustrated in **Figure 1**.

LiCl is capable of improving the diffusion rate of molten salts by facilitating the movement of ions.[30] The Li^+ ions play a crucial role in forming stable hydration structures, which contribute to a distinctive ionic environment.[31] This environment not only stabilizes the system but also influences reaction pathways at the operating temperature of 150 °C. Furthermore, the presence of LiCl enhances ion mobility and stabilizes the hydrated salt mixture, thereby synergistically promoting the selective A-site etching of the parent MAX phase. Meanwhile, the metal Mg^{2+} cations and the Cl^- anions in the solution function analogously to H^+ ions and F^- ions, respectively, similar to the chemical environment of HF etching.[7] Drawing inspiration from the MS^3 method for synthesizing MAX and MXene, we adopted the idea of using a low-temperature salt to etch the A layer from the MAX phase, the main difference between the synthesis method is listed in Table S1 (Supporting Information). Typically, a large amount of salt is required to synthesize MAX from the precursors, as a salt bed is necessary to prevent the material from coming into direct contact with air during synthesis. In the low-temperature salt etching method, the temperature is significantly lower than in traditional methods.[26] Compared to the conventional MS^3 LAMS etching approach, the present synthetic route employs a reduced

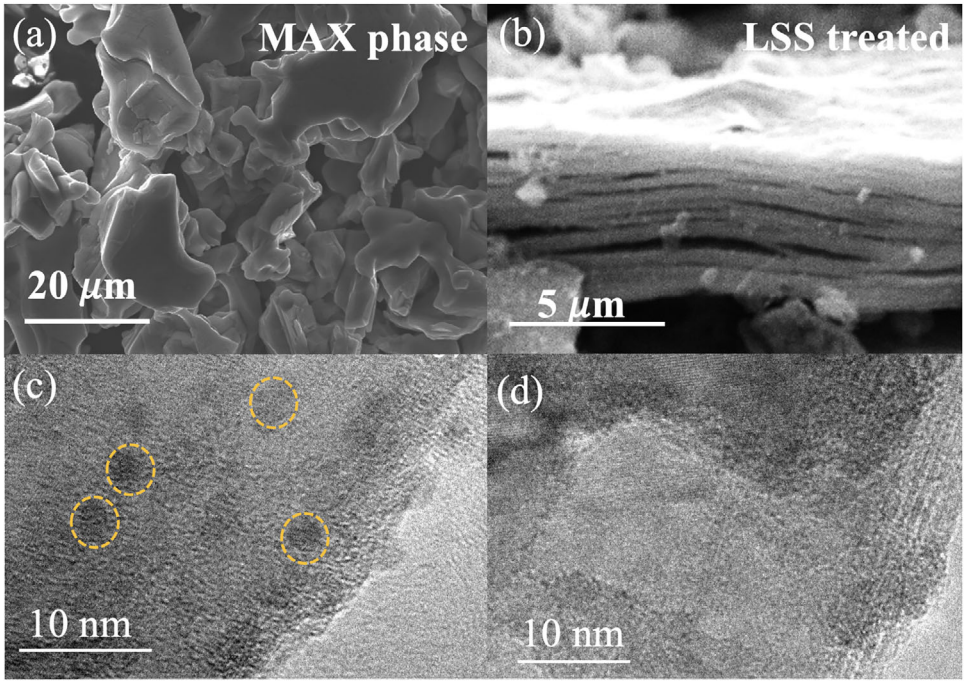

Figure 2. Morphological and structural characterizations of LSS-$Ti_3C_2T_x$ MXene. The SEM images of a) MAX phase material and b) LSS treated sample. c) The HRTEM image of the LSS-$Ti_3C_2T_x$ MXene sample before using dilute 2 M HCl washing and d) The HRTEM image of the LSS-$Ti_3C_2T_x$ MXene sample after washing and purification with dilute acid.

quantity of salts, with the mixed salt proportion to MAX phase equating to merely 60% – a stark contrast to the 500% salt proportion necessitated by the traditional salt-shielding etching methodology. Notably, an insufficient salt concentration in the conventional method can precipitate an incomplete reaction or etching failure.[18] After the reaction, the product is stirred in hot water (70 °C) to dissolve the remaining salt. The dissolved Li ions can disperse throughout the molten salt hydrate and reach the surface of the MXene during the process. After stirring, the mixture is thoroughly washed with 2 M HCl to remove the residual Mg metal, as reported in the previous study.[21] The quantitative yield of the MXene synthesis is ≈42%.

To demonstrate the MXene supernatants as a colloid, we illuminated the MXene supernatants with a red laser (Figure S1a, Supporting Information), highlighting its nano-colloidal properties through the Tyndall effect. Dynamic light scattering (DLS) and zeta potential analyses were conducted to investigate the adsorption properties of MXene. The MXene supernatant exhibited a DLS peak at ≈1.6 μm, while the LSS-$Ti_3C_2T_x$ samples displayed negative zeta potentials of −11 mV. Both the DLS and zeta potential results are consistent with previous findings and literature.[32] The etched MXene is collected and examined using scanning electron microscopy (SEM). The surface of the original MAX phase material is smooth with large lateral sizes (**Figure 2a**). When the etching temperature is kept above the melting point of the salt over an etching time of 12 h, a fracture appears on the surface of MXene (Figure 2b). The energy-dispersive X-ray spectroscopy (EDXs) result of the LSS-treated MXene indicates that only a small amount of Al is left in the MXene and it is terminated by =O and −Cl after the washing and etching process (Figure S2, Supporting Information). The oxygen is possibly attached to the surface of the MXene during the reaction and the washing process (Equation 1).

$$Ti_3AlC_2 + (y+3)/2MgCl_2 + (2x+z)/2H_2O \rightarrow Ti_3C_2(OH)_x(Cl)_y(O)_z + AlCl_3 + Mg - \text{basedbyproducts} \quad (1)$$

During the etching process, a redox reaction occurs where aluminum atoms lose electrons and transform into cations, and the magnesium cations gain electrons and transit into the metallic phase. High-resolution transmission electron microscopy (HRTEM) analysis confirmed the crystallinity and stoichiometry of LSS-$Ti_3C_2T_x$ MXene. Figure 2c illustrates the presence of Mg nanoparticles on the surface of MXene with a *d*-spacing of 0.320 nm (Figure S3, Supporting Information), consistent with the lattice parameter of Mg in the tetragonal phase. Due to the relatively small size of Mg nanoparticles, with an average diameter of 2.4 nm, the Mg nanoparticles can be easily removed by dilute acid. It is important to note that the metal nanoparticles produced using the previous etching approach typically have sizes >100 nm and hazardous solvents such as ammonium persulfate (APS) is applied to remove them.[7] Notably, the absence of APS in the LSS method, which is a strong oxidizing agent typically employed to remove metal particles, not only prevents the further oxidation of surface functional groups to TiO_2, but also avoids the safety concerns associated with handling such a potent oxidizing solution.[18] Thus, the easy removal of metal nanoparticles without using dangerous solvents or chemicals can give rise to high biocompatibility of our LSS-treated MXene, making it an ideal candidate in the biomedical sector.[33] After the acid treatment, no Mg nanoparticles can be observed on the surface of MXene

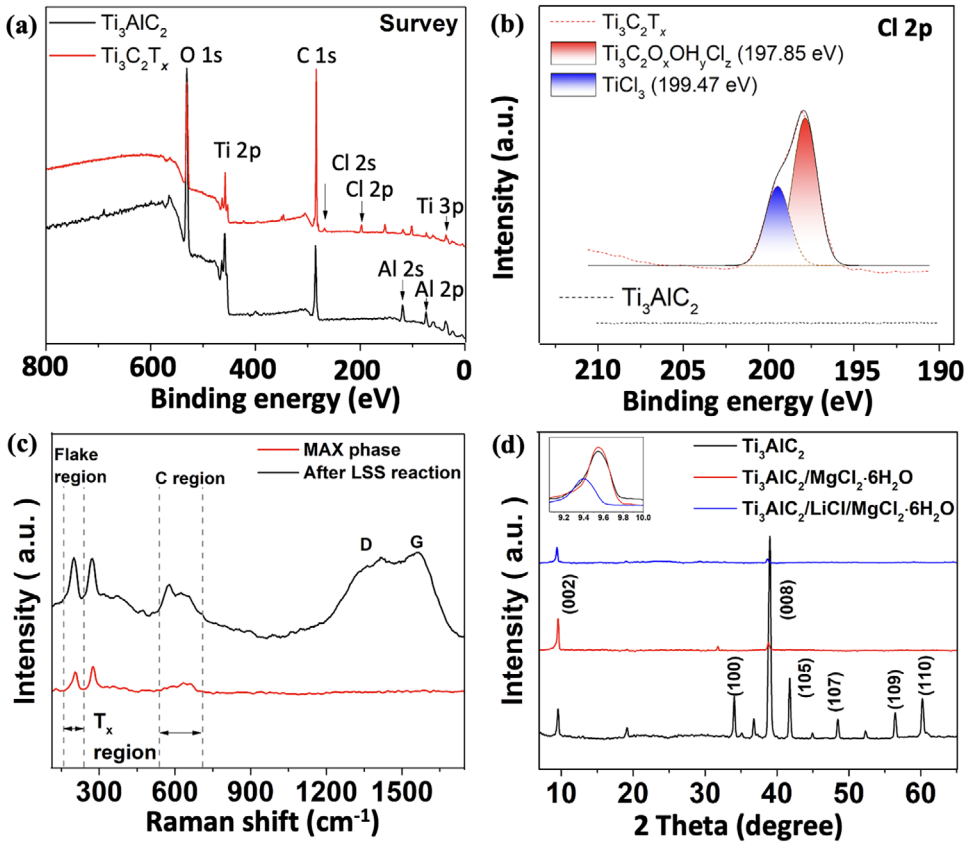

Figure 3. a) X-ray photoelectron spectroscopy (XPS) survey and b) high-resolution deconvoluted spectrum of $Ti_3C_2T_x$ on Cl 2p. c) The Raman spectra of the MXene and its MAX precursor. d) XRD patterns of pristine Ti_3AlC_2 and Ti_3AlC_2 treated with $LiCl/MgCl_2{\cdot}6H_2O$ and $MgCl_2{\cdot}6H_2O$, respectively.

(Figure 2d), as also confirmed with a distinct selected area electron diffraction (SAED) pattern (Figure S4, Supporting Information). The center-to-center *d*-spacing of 0.307 nm calculated from the TEM image corresponds to *a* lattice parameter of the material and matches well with the literature.[12]

2.2. Mechanism Investigation of the LSS Method

To investigate the influence of LiCl on LSS etching, the material at different stages of etching was analyzed structurally, morphologically, and spectroscopically. The water molecules present in $MgCl_2{\cdot}6H_2O$ serve as a source of oxygen and facilitate the reduction of aluminum and the formation of aluminum chloride ($AlCl_3$). Simultaneously, magnesium is formed through the reduction of $MgCl_2$.

LiCl can enhance the reaction by providing additional cations (Li^+) and acts as a reduction agent (Cl^-) source. These cations undergo ion exchange with $MgCl_2{\cdot}6H_2O$ and Al, potentially lowering the activation energy of the reaction and thus reducing the required reaction temperature. The elimination of use of LiCl in the etching process resulted in obvious variations in the morphology of the material, as shown in the SEM image (Figure S5, Supporting Information). A rough surface of the MAX phase material can be observed, indicating that the etching might only occur on the surface of the MAX material as the etching is incomplete,[34] and very few delamination are obtained. Besides, there is no notable improvement in the etching process even when the etching temperature is raised to 350 °C, which implies that 150 °C should be the optimal etching temperature. Further temperature increase shows no improvement on the etching efficiency and the use of LiCl during the etching reaction is crucial.

To investigate the surface chemistry of the synthesized MXenes, X-ray Photoelectron Spectroscopy (XPS) analyses are performed (**Figure 3a,b**). The XPS peaks at 197.9 and 199.5 eV in the XPS spectrum, attributed to the Cl 2p region, indicates the presence of chlorine as a functional group on the $Ti_3C_2T_x$ MXene surface. This suggests the potential for various chlorine terminations, such as —Cl or —Cl_2, which may coexist with other functional groups like =O or —OH. Notably, unlike the sharp peaks observed in MXene, the MAX phase shows no signal in the Cl 2p region, indicating that chlorine atoms are attached to the surface of MXene during the synthesis process.

The XPS spectrum of Ti_3AlC_2 reveals three prominent peaks in the C 1s region at 281.1, 284.7, and 286.2 eV, indicative of various carbon species within the material (Figure S6a, Supporting Information). The peak at 281.1 eV is attributed to carbon atoms in a metallic or carbide-like environment, reflecting strong M—C bonds that contribute to the structural stability of the MAX phase. The peak at 284.7 eV corresponds to carbon in a covalent bonding state, characteristic of the stable carbon framework within Ti_3AlC_2. The peak at 286.2 eV likely indicates the presence of

oxidized carbon species, suggesting slightly oxidation of the MAX phase material. In contrast, the XPS curves of MXene in C 1s region reveals three significant peaks at 283.8, 285.0, and 288.0 eV, which correspond to distinct functional groups on its surface. The peak at 283.8 eV indicates the presence of sp^2 hybridized carbon, suggesting graphitic or aromatic structures that enhance electronic properties. The peak at 285.0 eV reflects C—C and C—H bonds, pointing to alkyl groups and the primary carbon backbone, which is consistent with the literature values of ≈284.6 eV for C═C/C—C bonds.[35] The peak at 288.0 eV is associated with carbonyl and hydroxyl groups, indicating oxidized functionalities that enhance hydrophilicity and provide reactive sites for further modifications, corresponding to the —COOR groups (≈288.7 eV) described in previous studies.[35]

Furthermore, the XPS analysis of $Ti_3C_2T_x$ MXene in O 1s region reveals peaks at 531.3 eV and 531.6 eV, indicating specific functional groups on the surface (Figure S6b, Supporting Information). The peak at 531.3 eV is primarily attributed to hydroxyl groups (—OH) and possibly oxide species (Ti-O), which enhance the hydrophilicity and reactivity of the MXene. The peak at 531.6 eV likely corresponds to surface O terminations (~531.8 eV) as reported in previous studies,[35] and may also suggest the presence of other oxygen-containing groups. The analysis also shows two distinct O 1s peaks at 529.7 eV and 531.4 eV, providing insights into the MAX phase surface chemistry. The peak at 529.7 eV is attributed to oxygen in a stable environment, likely indicating Ti-O bonds characteristic of titanium oxides, suggesting strong interactions within the MAX phase. In contrast, the peak at 531.4 eV corresponds to less stable oxygen species, such as hydroxyl groups (—OH) or adsorbed water, reflecting moisture exposure of the MAX phase. The XPS results are consistent with the EDX and Raman spectroscopy findings, which reveal that surface functional groups are attached to the MXene after etching. It is suggested that ═O, —OH, and —Cl functional groups are present on the surface of the MXene.[36]

The X-ray diffraction (XRD) patterns and Raman spectra of both the as-synthesized MXene and its precursor were measured (Figure 3c,d) as a comparison for the reaction kinetics and mechanism investigation. The Ti_3AlC_2 sample holds the characteristic Raman peaks at 125, 204, 277, and 661 cm^{-1}, while the LSS-treated MXene demonstrates the featured peaks at 130, 199, 267, 398, and 573 cm^{-1}. The characteristic wavenumber associated with the vibrational modes of $Ti_3C_2T_x$ MXene materials can be divided into three distinct regions corresponding to the flake, surface functional groups, and carbon domains.[28] Specific wavenumbers at 130 and 199 cm^{-1} are attributed to titanium based species. Wavenumbers at 267 and 398 cm^{-1} correspond to in-plane hydroxyl terminations within the flake region, while the 573 cm^{-1} wavenumber is associated with ═O terminations on the carbon domains. XRD pattern indicates that the MXene is successfully etched from the MAX phase material. With the assistance of LiCl, the etching process was completed when the reaction temperature was maintained at 150 °C for 12 h. Moreover, the SEM structural characterizations clearly reveal a layered structure of the MXene. This result demonstrates that the LSS method not only can achieve selective etching of the MAX phase but also avoids the use of hazardous chemicals such as n-butyllithium[37] required in typical MXene intercalation and expansion processes, which is consistent with the previous report.[21]

To delve deeper into the fundamental mechanism of the etching process, *in-situ* Raman spectroscopy and XRD analysis were conducted (Figure S7, Supporting Information) and show the initial etching stage of the reaction. The sample is gradually heated *in-situ* at a rate of 10 °C per minute, and the XRD patterns are recorded in Figure S7a (Supporting Information). When the sample is heated to 50 °C, several XRD peaks are observed that are attributed to the $LiCl/MgCl_2{\cdot}6H_2O$ mixture, as compared to the simulated XRD pattern in Figure S8 (Supporting Information) and literature.[2] Upon heating to 110 °C, the 32° XRD peak vanishes while the characteristic peaks at 14.9°, 20.4°, 21.7°, and 30.5° – indexed to (110), (020), (111), and (201) planes of $MgCl_2{\cdot}6H_2O$ (PDF#25-0515)[38] – are analyzed to investigate the reaction between MAX phase and $LiCl/MgCl_2{\cdot}6H_2O$ (Figure S8c, Supporting Information). In the meantime, the interlayer spacing of the MAX is increased, and the peak corresponding to the (002) plane shifted from 9.60° to 9.48°. This change in structure suggests that lithium has been incorporated into the MAX structure, leading to a small shift in the (002) plane, indicating an enlarged interlayer spacing due to the selective removal of the Al component from the MAX phase precursor.[21] The *ex-situ* XRD show similar trend that the (002) plane is gradually shifted to a lower angle when the temperature increased from 70 to 150 °C (Figure S9, Supporting Information). It is worth noting that there is no observable change in the *in-situ* XRD patterns when the annealing temperature exceeds 150 °C. These results support the etching of MAX phase material initializing at 110 °C, which is to the melting temperature of $MgCl_2{\cdot}6H_2O$ (T_m = 117 °C), and the further decomposition of the $MgCl_2{\cdot}6H_2O$ is unfavorable to etching. The findings are consistent with the SEM results presented in Figure S5 (Supporting Information).

To investigate the rapid changes in the phase of the sample over the temperature range from 90–150 °C, *ex-situ* Raman spectroscopy measurements were conducted on various samples. The Raman spectra suggest significant changes in the surface functional groups occurred between 90 and 110 °C, with the formation of additional peaks corresponding to ═O functional groups in the T_x and C regions, accompanied by an increased TiO_2 signal. This TiO_2 likely originates from oxidation of the MAX phase material and is eliminated after washing with 2 M HCl, as shown in Figures 3c; S6 (Supporting Information). As the temperature further increased from 110 to 150 °C, the signals attributed to ═O functional groups and TiO_2 vanishes, and that of the —OH functional groups become predominant. The differential scanning calorimetry (DSC) pattern and thermal gravity analysis (TGA) in Figure S10 (Supporting Information) indicates that the $MgCl_2{\cdot}6H_2O$ begins to lose its structural water at 118 °C, as described in Equations (2 and 3):

$$MgCl_2 \cdot 6H_2O = MgCl_2 \cdot 4H_2O + 2H_2O\,(96 - 117\ ^\circ C) \quad (2)$$

$$MgCl_2 \cdot 4H_2O \rightarrow MgCl_2 \cdot 2H_2O + 2H_2O\,(135 - 180\ ^\circ C) \quad (3)$$

It is noted that pure anhydrous $MgCl_2$ and LiCl have high melting points of 714 and 605 °C, respectively, and their eutectic mixture (1:1 ratio) exhibits a significantly lower melting temperature of ≈440 °C. This reduction in melting

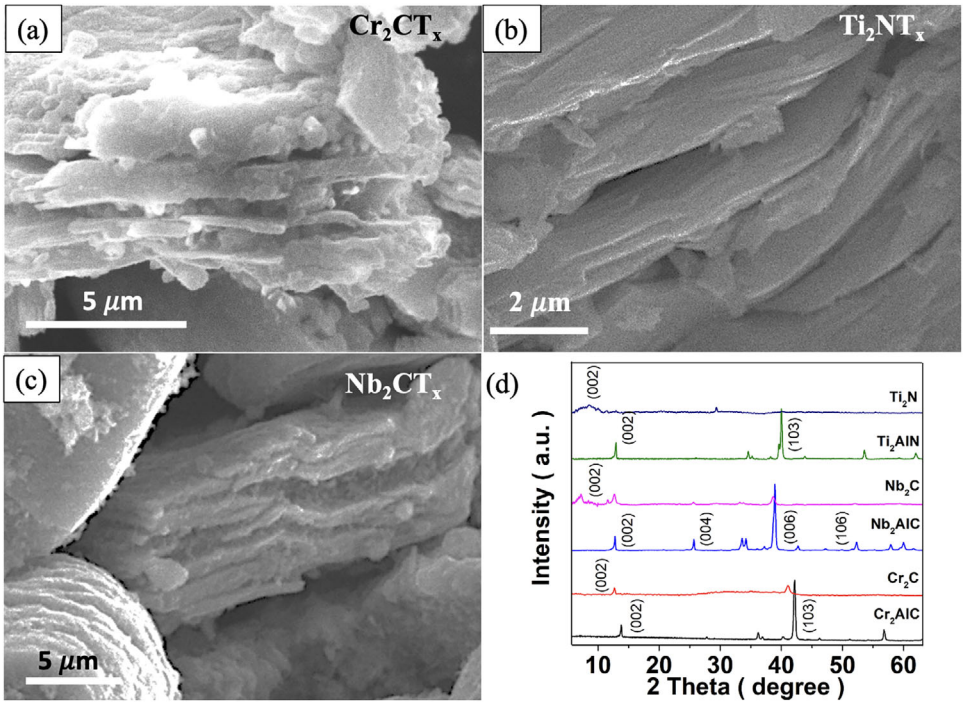

Figure 4. SEM images of a) Cr_2CT_x, b) Ti_2NT_x, and c) Nb_2CT_x after the LSS reaction and delamination process. d) The XRD curves of the various samples before and after the reaction.

temperature demonstrates the effective formation of a eutectic system.[39] On the other hand, the LiCl-$MgCl_2$-H_2O system exhibits intriguing physicochemical properties as a molten salt hydrate. In this system, Li^+ ions demonstrate unique characteristics that its strong hydration effects influencing both the first and second coordination shell water molecules.[40] To investigate the heating behavior of the $MgCl_2{\cdot}6H_2O$/LiCl mixture salt, we conducted TG-DSC measurements on both $MgCl_2{\cdot}6H_2O$ alone and the $MgCl_2{\cdot}6H_2O$/LiCl mixture. Notably, $MgCl_2{\cdot}6H_2O$ alone showed significant weight loss, indicating rapid dehydration, while the $MgCl_2{\cdot}6H_2O$/LiCl mixture exhibited a slower rate of weight loss. This suggests that the presence of LiCl helps retain the hydrated state of $MgCl_2{\cdot}6H_2O$, and form a protective layer on the top of the mixture. That unique environment provides a suitable condition for etching. Experimental observations support this mechanism, demonstrated by the solidified salt layer and dark residues at the bottom of the annealed product. These findings indicate a non-traditional molten behavior wherein the reaction proceeds in a semi-molten state significantly below the melting point of the anhydrous salt. (Figure S10, Supporting Information). Combined analyses of SEM, Raman spectroscopy, DSC, and XRD indicate that the shielded salt melts at approximately 118 °C, near the melting point of $MgCl_2{\cdot}6H_2O$ (T_m = 117 °C). Below this temperature, the material is etched without the protective cover of the salt. Beneficially, the low-temperature reaction conditions prevent the material from undergoing serious oxidation but instead increase the O_2 functionalization on the surface at temperatures lower than the melting point of the salt (90–110 °C). After the melting point of the salt is reached, the shielded salt protects the MAX phase material and reduces the introduction of oxygen during the etching process, resulting in only hydroxyl groups being attached to the material surface. These results also suggest that our LSS method is distinct from the conventional MS^3 approach, which can effectively prevent over-oxidation due to the insufficient shielding and incomplete pressing of the material appeared in the MS^3 method.

2.3. Approach Extended to Other MXenes and Demonstration of MXene for Energy Applications

To examine the universality and generality of the low-temperature etching method, MAX phase materials theoretically predicted to be hard to exfoliate were investigated.[13,22] Theoretically, the synthesis of Cr-based carbides is more challenging compared to Ti-, Nb-, or V-based carbides. This is due to the stronger M—A bonding (as indicated by higher Bader charges on the M atoms), higher formation energy, and challenges associated with HF etching. When subjected to HF etching, these MAX phases either resist selective Al removal or undergo complete structural dissolution within hours.[41] Here, Cr_2CT_x, Nb_2CT_x, and Ti_2NT_x were etched from Cr_2AlC, Nb_2AlC, and Ti_2AlN MAX phase materials, respectively. Identical etching condition for the Ti_3AlC_2 was adopted on these MAX phase materials. The SEM images and XRD patterns of **Figure 4** indicate the selective etching of the Al layer from the various MAX phase materials.[2,42–44]

After the LSS reaction, new peaks are formed at 7.55° and 7.31° for Ti_2NT_x and Nb_2CT_x, respectively, due to the intercalation in the washing process (Figure S11, Supporting Information). This observation implies the exfoliation of these hard-to-exfoliate MXenes. It is worth noting that no additional intercalator is used in

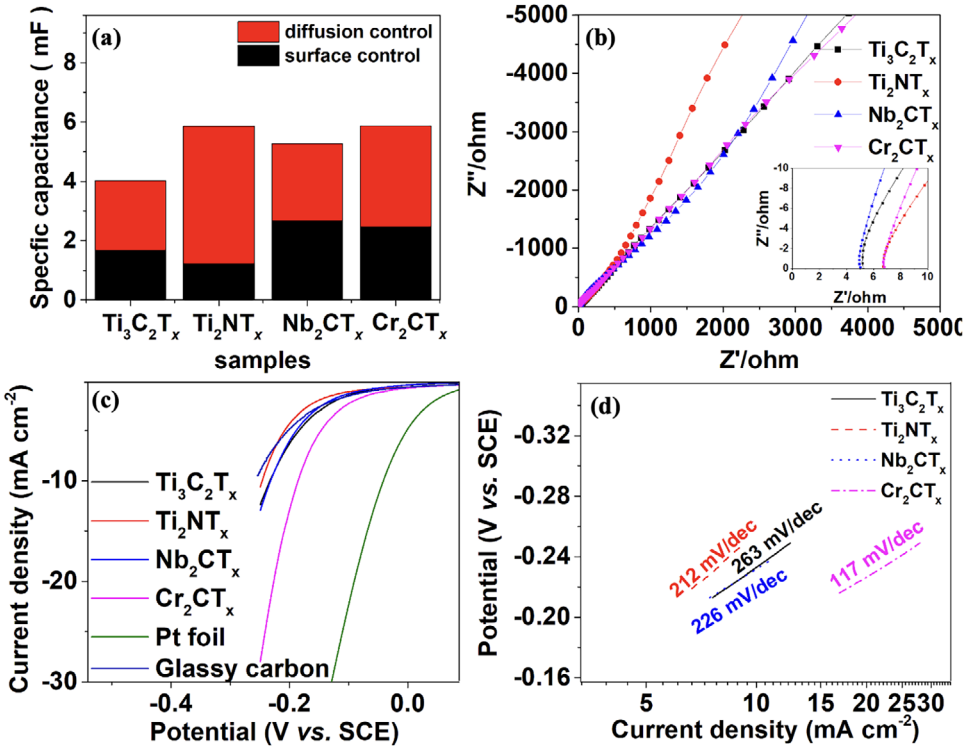

Figure 5. a) The kinetics analysis of $Ti_3C_2T_x$, Ti_2NT_x, Nb_2CT_x, and Cr_2CT_x samples. b) EIS of the various catalysts. c) The LSV for the LSS-etched sample in an acidic solution and d) the corresponding Tafel plot.

the sonication exfoliation process. The shifted (002) planes in the XRD indicate the *d*-spacing of 1.17 and 1.21 for the LSS-treated Ti_2NT_x and Nb_2CT_x, respectively, with a van der Waals (vdW) gap of 0.270 nm. The MAX residue remained before the purification process of MXene. The material is subsequently treated by sonication, centrifugation, and filtration to separate MXene from the unetched MAX phase material. The different bonding energies among the samples result in distinct (002) peak broadening and shifting patterns for Ti_2NT_x, Nb_2CT_x, and Cr_2CT_x. Ti_2NT_x exhibits characteristic peak broadening at 7.55°, while Nb_2CT_x shows a notable peak shift from the original (002) peak at 11.8° to new positions at 7.13° and 11.5° – behavior typically observed in hard-to-exfoliate MXenes.[45] For Cr_2CT_x, XRD analysis reveals a significant peak shift from 13.8° to 12.7°, which correlates with its distinctive accordion-like morphology in SEM image. Supporting these XRD findings, EDX analysis (Figure S12, Supporting Information) confirms the selective etching of Al from all MAX phase materials, with Cr_2CT_x samples showing particularly low Al signals, validating the successful synthesis process.

As a proof-of-concept experiment, the LSS-synthesized MXene nanoflakes derived from the MAX phase precursor were further prepared as electrodes by drop-casting MXenes on a glassy carbon electrode without any additive. Figure S13a (Supporting Information) shows the cyclic voltammetry profile of the LSS-etched MXene electrodes in 0.5 M H_2SO_4 solution recorded at 10 mVs^{-1}. **Figure** 5a illustrates the capacitance of $Ti_3C_2T_x$, Ti_2NT_x, Nb_2CT_x, and Cr_2CT_x are 4.04, 5.80, 5.31, and 5.86 mF, respectively. The kinetics analysis (Figure S13b, Supporting Information) indicates that at a scan rate of 10 mV s^{-1}, the surface capacitance of Cr_2CT_x is measured to be 2.46 mF, while the diffusion-controlled capacitance is 3.40 mF. Furthermore, the surface capacitance contributes to 42.0% of the total capacitance, suggesting that Cr_2CT_x possesses the largest electrochemical active surface area (ECSA) among the different MXenes studied. The ECSA is closely related to surface-controlled capacitance and the increase in ECSA plays a crucial role in enhancing the HER activity. The observed enhancement in ECSA is due to the synergistic effect of the delaminated MXene, which results in the generation of a greater number of catalytically active sites for efficient hydrogen production. The specific capacitances responsible for C_{dif} and C_{cap} were estimated for the mechanism studies.

$$C_{total} = A_1 + A_2 \nu^{-0.5} \quad (4)$$

$$C_{total} = C_{cap} + C_{dif} \quad (5)$$

where C_{total}, $C_{cap,}$ and C_{dif} are the total capacitance, capacitive capacitance (or ECSA), and diffusion-controlled capacitance of the MXene, respectively; A_1 and A_2 are constants while ν is the scan rate. The enhanced conductivity of the system was investigated using electrochemical impedance spectroscopy (EIS), as depicted in Figure 5b. The high-frequency tail with a steeper slope suggests a reduced Warburg resistance at the solid/liquid interface. The contact resistance of the electrode is reduced from 9 Ohms of the glassy carbon electrode (Figure S14, Supporting Information) to 5.15, 7.25, 5.36, and 7.21 Ohms for $Ti_3C_2T_x$, Ti_2NT_x, $Nb_2CT_{x,}$ and Cr_2CT_x, respectively. The substantial reduction in contact resistance suggests that the MXene material exhibits high

electrical conductivity. $Ti_3C_2T_x$, Ti_2NT_x, and Nb_2CT_x exhibit overpotentials of 234, 246, and 236 mV at the current density of 10 mA cm^{-2}, as shown in Figure 5c. Notably, the Cr_2CT_x MXene demonstrated a remarkably low overpotential of 186 mV at the current density of 10 mA cm^{-2}, benefiting from its fast kinetics, low internal resistance, and enlarged ECSA. Furthermore, the Cr_2CT_x theoretically possesses high catalytic properties.[46] We hypothesize that the unique surface terminations and the optimized conductivity of our synthesized Cr_2CT_x MXenes synergistically enhance their HER performance. The spontaneous delamination achieved without hazardous intercalants results in MXenes with less oxidation and more =O functional groups. This is particularly important for catalytic applications where active site accessibility determines performance. It is noted that Ti_2NT_x has a capacitance comparable to Cr_2CT_x and the surface capacitance accounts for only 20.9% of the total capacitance, leading to a mediocre HER activity. The functionalized Cr_2CT_x ranks as a good catalyst compared to existing materials, such as 1D $Ti_3C_2T_x$ nanowire,[47] as summarized in Table S2 (Supporting Information). The Tafel plot (Figure 5d) exhibits a consistent agreement with the kinetic analysis as denoted by a decreased slope, which is indicative of fast kinetics. This reduced slope can be attributed to the favorable morphology of the material, which enables high ion accessibility, and the low contact resistance between the electrode and the electrolyte. The kinetics analysis, in conjunction with the Raman spectroscopy results, illustrate that the functionalization of the MXene is beneficial for HER performance. This proof-of-concept demonstration highlights the merits of the LSS-treated MXene which exhibit favorable surface kinetics and illustrate comparable electrocatalytic performance to traditional MXene delaminated from common intercalants.

3. Conclusion

In conclusion, the proposed LSS etching method enables safe, simple, and non-toxic MXene synthesis in ambient air at remarkably low temperatures of 150 °C. The low reaction temperature can be readily achieved with just a muffle furnace or conventional hot plate. This approach inhibits the oxidation of the MXene surface to TiO_2 by eliminating the use of oxidizing washing agents and the utilization of high temperature. More importantly, this method expands the producible range of LAMS-etched MXenes, including Cr_2CT_x, Nb_2CT_x, and Ti_2NT_x that are typically difficult to etch. The fabrication of MXene through sonication within dilute acid gets rid of using toxic or corrosive agents. Comprehensive investigation reveals that LiCl serves essential functions: enhancing diffusion rate and functioning as an intercalant. In particular, LSS-treated Cr_2CT_x MXene exhibits exceptional electrocatalytic performance with a low overpotential of 186 mV at a current density of 10 mA cm^{-2}, benefiting from its fast kinetics, low internal resistance, and enlarged ECSA. The proposed LSS method presents dominant advances in the field of MXene synthesis and associated applications. Furthermore, the fully toxic-free nature of the LSS fabrication routes enriches the functionalities of MXenes as promising materials for widespread applications, including electrochemical and biomedical sectors.

4. Experimental Section

Materials and Reagents: Titanium aluminum carbide, chromium aluminum carbide, titanium aluminum nitride, and niobium aluminum carbide (200 mesh, 99 percent purity) were acquired from Nanjing Mission New Material Co., Ltd. Sigma supplied the hydrochloride acid, Magnesium chloride hexahydrate, lithium chloride, and sulfuric acid. All materials were utilized as received, with no further purification.

Synthesis of MXene: The synthesis is conducted in a muffle furnace without the use of inert gas for protection. 1 g of MAX phase material is mixed with 1 g of magnesium chloride hexahydrate and 1 g of lithium chloride in a 10 mL aluminum oxide crucible. After several hours of etching, the MXene is first washed with ethanol and deionized water (D.I. water), and centrifuged at 2000 rpm for 5 min to remove the unreacted and insoluble magnesium chloride hexahydrate salt. The etched product is washed with diluted HCl to remove the Mg and Al particles. 2 M of HCl is mixed with ethanol and used to further remove the impurities. The final product is washed with D.I. water.

Delamination and Collection of the MXene: The MXene is collected by the method as reported in the literature.[48] For the soft delamination process and purification of the MXene, the solution was allowed to settle undisturbed for 1 h to facilitate the precipitation of multilayer MXene particles. A 50 mL centrifuge tube was replenished with D.I. water, and the MXene was redispersed by inverting and vertexing the vial several times. This procedure was repeated for several cycles until the MXene spontaneously delaminated, resulting in a darkened solution. The darkened solution is centrifuged for 5 min in 10 000 r.p.m. and collected for further characterization.

DFT Calculation for Lattice Structure: The charge density and electronic properties of MXene were calculated using the CAmbridge Serial Total Energy Package (CASTEP) simulation code.[49] The Perdew-Burke-Ernzerhof (PBE) generalized gradient approximation (GGA) was selected for the exchange-correlation functional, and a set of norm-conserving pseudopotentials was employed in the calculation The kinetic energy cutoff for the plane wave is 700 eV, and a vacuum layer of 15 Å is utilized. Only the x and y dimensions change for MXene cell optimization and relaxation (i.e., 2D xy constraint). The dipole and vdW interactions were taken into account. A 12 × 12 × 1 Monkhorst *k*-point grid was utilized for MXenes. Vesta is used for visualizing the XRD pattern of the material.[50]

Supporting Information

Supporting Information is available from the Wiley Online Library or from the author.

Acknowledgements

This work was supported by the grants from the Research Grants Council of Hong Kong GRF No. 15303123, PDFS2324-5S09 and HKPFS No. PF20-46080, PolyU SRFS2122-5S02, AoE/P-701/20, PolyU Projects of RCNN 1-CE0H and 1-YWC0.

Conflict of Interest

The authors declare no conflict of interest.

Data Availability Statement

The data that support the findings of this study are available from the corresponding author upon reasonable request.

Keywords

2D materials, electrocatalysts, molten salts hydrates, MXenes

Received: February 23, 2025
Revised: April 1, 2025
Published online: April 14, 2025

[1] Y. Gogotsi, B. Anasori, *ACS Nano* **2019**, *13*, 8491.
[2] S.-Y. Pang, Y.-T. Wong, S. Yuan, Y. Liu, M.-K. Tsang, Z. Yang, H. Huang, W.-T. Wong, J. Hao, *J. Am. Chem. Soc.* **2019**, *141*, 9610.
[3] M. Song, S. Y. Pang, F. Guo, M. C. Wong, J. Hao, *Adv. Sci.* **2020**, *7*, 2001546.
[4] Y. Wang, Y. Yue, F. Cheng, Y. Cheng, B. Ge, N. Liu, Y. Gao, *ACS Nano* **2022**, *16*, 1734.
[5] S.-Y. Pang, W. F. Io, F. Guo, Y. Zhao, J. Hao, *Materials Science and Engineering: R: Reports* **2025**, *163*, 100894.
[6] T. Li, L. Yao, Q. Liu, J. Gu, R. Luo, J. Li, X. Yan, W. Wang, P. Liu, B. Chen, W. Zhang, W. Abbas, R. Naz, D. Zhang, *Angew. Chem., Int. Ed.* **2018**, *57*, 6115.
[7] Y. Li, H. Shao, Z. Lin, J. Lu, L. Liu, B. Duployer, P. O. Å. Persson, P. Eklund, L. Hultman, M. Li, K. Chen, X.-H. Zha, S. Du, P. Rozier, Z. Chai, E. Raymundo-Piñero, P.-L. Taberna, P. Simon, Q. Huang, *Nat. Mater.* **2020**, *19*, 894.
[8] M. Naguib, M. Kurtoglu, V. Presser, J. Lu, J. Niu, M. Heon, L. Hultman, Y. Gogotsi, M. W. Barsoum, *Adv. Mater.* **2011**, *23*, 4248.
[9] S. Wang, Y. Liu, K. Lu, W. Cai, Y. Jie, F. Huang, X. Li, R. Cao, S. Jiao, *Energy & Fuels* **2021**, *35*, 4587.
[10] Z. Wang, Z. Xu, H. Huang, X. Chu, Y. Xie, D. Xiong, C. Yan, H. Zhao, H. Zhang, W. Yang, *ACS Nano* **2020**, *14*, 4916.
[11] M. Mozafari, M. Soroush, *Mater. Adv.* **2021**.
[12] V. Kamysbayev, A. S. Filatov, H. Hu, X. Rui, F. Lagunas, D. Wang, R. F. Klie, D. V. Talapin, *Science* **2020**, *369*, 979.
[13] B. Anasori, M. R. Lukatskaya, Y. Gogotsi, *Nat. Rev. Mater.* **2017**, *2*, 16098.
[14] M. Özcan, A. Allahbeickaraghi, M. Dündar, *Clinical oral investigations* **2012**, *16*, 15.
[15] C. E. Shuck, K. Ventura-Martinez, A. Goad, S. Uzun, M. Shekhirev, Y. Gogotsi, *ACS Chemical Health & Safety* **2021**, *28*, 326.
[16] M. Shen, W. Jiang, K. Liang, S. Zhao, R. Tang, L. Zhang, J. Q. Wang, *Angew. Chem.* **2021**, *133*, 27219.
[17] J. Zhu, F. Li, Y. Hou, H. Li, D. Xu, J. Tan, J. Du, S. Wang, Z. Liu, H. Wu, F. Wang, Y. Su, H.-M. Cheng, *Nat. Mater.* **2024**, *23*, 604.
[18] X. Liu, Y. Li, H. Ding, L. Chen, S. Du, Z. Chai, Q. Huang, *Journal of Materiomics* **2023**, *9*, 1032.
[19] K. Arole, J. W. Blivin, A. M. Bruce, S. Athavale, I. J. Echols, H. Cao, Z. Tan, M. Radovic, J. L. Lutkenhaus, M. J. Green, *Chem. Commun.* **2022**, *58*, 10202.
[20] L. Liu, M. Orbay, S. Luo, S. Duluard, H. Shao, J. Harmel, P. Rozier, P.-L. Taberna, P. Simon, *ACS Nano* **2021**, *16*, 111.
[21] T. Zhang, K. Shevchuk, R. J. Wang, H. Kim, J. Hourani, Y. Gogotsi, *Chem. Mater.* **2024**.
[22] N. C. Frey, J. Wang, G. I. n. Vega Bellido, B. Anasori, Y. Gogotsi, V. B. Shenoy, *ACS Nano* **2019**, *13*, 3031.
[23] A. Dash, R. Vaßen, O. Guillon, J. Gonzalez-Julian, *Nat. Mater.* **2019**, *18*, 465.
[24] J. Chen, Q. Jin, Y. Li, H. Shao, P. Liu, Y. Liu, P. L. Taberna, Q. Huang, Z. Lin, P. Simon, *Energy & Environmental Materials* **2022**, *6*, e12328.
[25] Z. Li, K. Li, Y. Li, Y. Yu, J. Lv, X. Liu, K. Guan, W. Lei, S. Zhang, H. Zhang, *Adv. Funct. Mater.* **2023**, 2310371.
[26] G. Ma, H. Shao, J. Xu, Y. Liu, Q. Huang, P.-L. Taberna, P. Simon, Z. Lin, *Nat. Commun.* **2021**, *12*, 1.
[27] Y. Wang, B. Zhou, Q. Tang, Y. Yang, B. Pu, J. Bai, J. Xu, Q. Feng, Y. Liu, W. Yang, *Adv. Mater.* **2024**, *36*, 2410736.
[28] A. Sarycheva, Y. Gogotsi, *Chem. Mater.* **2020**, *32*, 3480.
[29] M.-Q. Zhao, C. E. Ren, Z. Ling, M. R. Lukatskaya, C. Zhang, K. L. Van Aken, M. W. Barsoum, Y. Gogotsi, *Adv. Mater.* **2014**, 27.
[30] H. Nadimi, M. Soltanieh, H. Sarpoolaky, *Ceram. Int.* **2020**, *46*, 18725.
[31] Y. Liu, H. Huang, R. Tang, L. Han, J. Yang, M. Xu, M. Ge, Y. Tang, X. Fu, H. Liu, Y. Qian, *Phys. Chem. Chem. Phys.* **2021**, *23*, 20489.
[32] K. Maleski, C. E. Ren, M.-Q. Zhao, B. Anasori, Y. Gogotsi, *ACS Appl. Mater. Interfaces* **2018**, *10*, 24491.
[33] J. Yoon, S. Kim, K. H. Park, S. Lee, S. J. Kim, H. Lee, T. Oh, C. M. Koo, *Small Methods* **2023**, *7*, 2201579.
[34] L. T. Alameda, C. F. Holder, J. L. Fenton, R. E. Schaak, *Chem. Mater.* **2017**, *29*, 8953.
[35] Y. Wang, Y. Cui, D. Kong, X. Wang, B. Li, T. Cai, X. Li, J. Xu, Y. Li, Y. Yan, H. Hu, M. Wu, Q. Xue, Z. Yan, L. Zhao, W. Xing, *Carbon* **2021**, *180*, 118.
[36] Y. Li, H. Shao, Z. Lin, J. Lu, L. Liu, B. Duployer, P. O. Å. Persson, P. Eklund, L. Hultman, M. Li, K. Chen, X.-H. Zha, S. Du, P. Rozier, Z. Chai, E. Raymundo-Piñero, P.-L. Taberna, P. Simon, Q. Huang, *Nat. Mater.* **2020**, *19*, 894.
[37] X. Chen, Y. Zhu, M. Zhang, J. Sui, W. Peng, Y. Li, G. Zhang, F. Zhang, X. Fan, *ACS Nano* **2019**, *13*, 9449.
[38] A. Ur Rehman, T. Zhao, I. Muhammad, S. Rasheed, R. Shah, A. R. Altaf, F. Zhang, S. Yun, *J. Energy Storage* **2023**, *59*, 106509.
[39] F. Zhu, L. Li, X. Cheng, S. Ma, L. Jiang, K. Qiu, *Electrochim. Acta* **2020**, *357*, 136867.
[40] H. Ge, Y. Zhao, H. Yang, M. Wang, *Spectrochim. Acta, Part A* **2022**, *267*, 120543.
[41] N. C. Frey, J. Wang, G. I. Vega Bellido, B. Anasori, Y. Gogotsi, V. B. Shenoy, *ACS Nano* **2019**, *13*, 3031.
[42] S.-Y. Pang, W.-F. Io, L.-W. Wong, J. Zhao, J. Hao, *Adv. Sci.* **2020**, *7*, 1903680.
[43] H. Lin, S. Gao, C. Dai, Y. Chen, J. Shi, *J. Am. Chem. Soc.* **2017**, *139*, 16235.
[44] T. Y. Ma, J. L. Cao, M. Jaroniec, S. Z. Qiao, *Angew. Chem., Int. Ed.* **2016**, *55*, 1138.
[45] M. Naguib, J. Halim, J. Lu, K. M. Cook, L. Hultman, Y. Gogotsi, M. W. Barsoum, *J. Am. Chem. Soc.* **2013**, *135*, 15966.
[46] Y. Cheng, L. Wang, Y. Li, Y. Song, Y. Zhang, *J. Phys. Chem. C* **2019**, *123*, 15629.
[47] W. Yuan, L. Cheng, Y. An, H. Wu, N. Yao, X. Fan, X. Guo, *ACS Sustainable Chem. Eng.* **2018**, *6*, 8976.
[48] M. Shekhirev, J. Busa, C. E. Shuck, A. Torres, S. Bagheri, A. Sinitskii, Y. Gogotsi, *ACS Nano* **2022**, *16*, 13695.
[49] S. J. Clark, M. D. Segall, C. J. Pickard, P. J. Hasnip, M. I. Probert, K. Refson, M. C. Payne, *Zeitschrift für kristallographie-crystalline materials* **2005**, *220*, 567.
[50] K. Momma, F. Izumi, *J. Appl. Crystallogr.* **2011**, *44*, 1272.